Chemistry–A European Journal
Research Article
doi.org/10.1002/chem.202202382
Chemistry Europe
European Chemical Societies Publishing
www.chemeurj.org

Chemical Strategies for Dendritic Magneto-plasmonic Nanostructures Applied to Surface-Enhanced Raman Spectroscopy

Tiago Fernandes,[a] Helena I. S. Nogueira,[a] Carlos O. Amorim,[b] João S. Amaral,[b] Ana L. Daniel-da-Silva,[a] and Tito Trindade*[a]

Abstract: Chemical analyses in the field using surface-enhanced Raman scattering (SERS) protocols are expected to be part of several analytical procedures applied to water quality monitoring. To date, these endeavors have been supported by developments in SERS substrate nanofabrication, instrumentation portability, and the internet of things. Here, we report distinct chemical strategies for preparing magneto-plasmonic (Fe_3O_4:Au) colloids, which are relevant in the context of trace-level detection of water contaminants due to their inherent multifunctionality. The main objective of this research is to investigate the role of poly(amidoamine) dendrimers (PAMAMs) in the preparation of SERS substrates integrating both functionalities into single nanostructures. Three chemical routes were investigated to design magneto-plasmonic nanostructures that translate into different ways for assessing SERS detection by using distinct interfaces. Hence, a series of magneto-plasmonic colloids have been characterized and then assessed for their SERS activity by using a model pesticide (thiram) dissolved in aqueous samples.

Introduction

In recent years, many strategies have been reported for designing multifunctional systems that combine the physicochemical properties of two different materials in a single-nanostructure. A particular interest in preparing magneto-plasmonic systems, which intertwine magnetic properties with their plasmonic activity, has emerged.[1] Magneto-plasmonic nanomaterials present a set of promising properties to be explored in several areas, such as biomedicine or sensing.[2] Their development has attracted significant attention in recent years as probing platforms for trace-level detection of chemical species through surface-enhanced Raman scattering (SERS).[3] SERS has been extensively used for probing analytes at ultra-low concentrations by taking advantage of the intensification of the Raman signal when a target analyte adsorbs onto (or is near) the surface of metals with localized surface plasmon resonances (LSPR). Consequently, the coupling of the magnetic component to the plasmonic counterpart has several advantages for SERS probing. For instance, it offers the ability to improve SERS signal sensitivity by preconcentrating a target analyte through magnetic separation and subsequent measurements in a single substrate.[4]

Gold nanoparticles have been extensively investigated in plasmonics, due to tunable plasmonic response as function of size and shape, resulting in unique optical profiles such as Mie scattering, surface plasmon resonance (SPR), surface-enhanced fluorescence, and surface Raman scattering.[2a,5] Moreover, the high chemical stability of Au nanoparticles, along with the ability to functionalize their surface with an extensive library of functional groups, are advantageous for developing versatile magneto-plasmonic nanostructures.[6] Concerning the magnetic phases, common magneto-plasmonic materials involve transition metals, such as Fe, Co, or Ni, or their alloys.[7] However, such magnetic nanometals are prone to oxidation and require additional surface coatings to avoid degradation of their physicochemical properties.[7] An alternative approach relies on the combination of a noble metal (e.g., Au) with a magnetic metal oxide such as magnetite (Fe_3O_4).[1,2b,8] Indeed, Fe_3O_4 nanoparticles have been used in several applications due to their well-established chemical synthesis, allowing the preparation of nanoparticles with morphological dependent magnetic properties.[9] However, the number of chemical methods available for preparing such multifunctional particles is still limited, with the chemists facing several challenges in the

[a] Dr. T. Fernandes, Prof. H. I. S. Nogueira, Dr. A. L. Daniel-da-Silva, Prof. T. Trindade
Department of Chemistry, CICECO – Aveiro Institute of Materials
University of Aveiro
3810-193 Aveiro (Portugal)
E-mail: tito@ua.pt

[b] Dr. C. O. Amorim, Dr. J. S. Amaral
Department of Physics, CICECO – Aveiro Institute of Materials
University of Aveiro
3810-193 Aveiro (Portugal)

Supporting information for this article is available on the WWW under https://doi.org/10.1002/chem.202202382

Part of a Special Collection for the 8thEuChemSChemistry Congress 2022 consisting of contributions from selected speakers and conveners. To view the complete collection, visit 8th EuChemS Chemistry Congress.

search of stable magneto-plasmonic structures. On the other hand, the extensive library of strategies for their surface functionalization offers an open field for exploring new strategies towards multifunctional materials, namely colloidal magneto-plasmonic nanostructures.[10] For example, a typical procedure involves the silica coating of the magnetic phase, increasing the chemical robustness of the magnetic core while providing additional surface derivatization ability for attaching plasmonic particles.[2b,9b] Chemical strategies for controlling the final properties of more complex magneto-plasmonic nanostructures require merging synthetic routes and surface modification methods usually employed in distinct contexts. As an illustrative example of this integrated strategy is the recent report by Mehdipour et al., describing the flow-based synthesis of magneto-plasmonic nanoparticles comprising gold and silica-coated iron oxide nanoparticles.[11]

Dendrimers have been employed as basic building blocks for designing several types of nanoarchitectures.[12] Among this class of polymers, poly(amidoamine) (PAMAM) dendrimers are commercially available with well-defined sizes depending on the required generation. Moreover, the high number of end groups of PAMAM dendrimers and the ability to tune their surface chemistry allow their incorporation in different hybrid materials, thus making them good candidates for exploring their integration in magneto-plasmonic nanostructures.[13] Saedi et al. have reported the synthesis of Fe_3O_4 nanoparticles modified by third generation PAMAM dendrimers grown in situ, through the convergent approach at the surface of the magnetic particles.[13h] The resulting magnetic hybrid material was then used to incorporate Ag nanoparticles in the interior of the dendrimer, to produce a series of carrageenan-based nanocomposites with antibacterial activity. Ma et al. have reported the synthesis of multifunctional Fe_3O_4/P(MMA-DVB)/PAMAM/Au microspheres, where third generation PAMAM dendrimers were grown at the surface of magnetite and then used for the incorporation of Au nanoparticles in the void spaces of the dendrimer. The resulting hybrid material was investigated in the catalytic conversion of 4-nitrophenol, displaying good performance for at least ten cycles.[14] Kannappan et al. described the preparation of Fe_3O_4@SiO_2-PAMAM nanohybrids which were then used as templates for the encapsulation of Au nanoparticles. The ensuing magnetically recyclable hybrids were then used for the selective oxidation of alcohols, displaying good efficiency for at least five cycles.[15] Cai et al. reported the facile synthesis of Fe_3O_4@Au nanocomposite particles as dual-mode contrast agents for magnetic resonance and computed tomography imaging applications.[16]

Unlike the methods reported so far, where the dendrimer is grown in situ at the surface of magnetic nanoparticles, we wish to report here distinct alternative strategies for coating magnetite with fifth generation PAMAM dendrimers. The resulting magnetic hybrid materials were then investigated as platforms to produce magneto-plasmonic nanostructures using the dendrimer as an essential chemical in defining the multifunctionality of the final materials. The ensuing dendrimer-based materials were then investigated as SERS substrates for detecting a model pesticide in water, discussing the context of potential application for each type of magneto-plasmonic nanostructure proposed here.

Results and Discussion

Synthesis of dendrimer-based magnetite nanomaterials

In this research, several strategies are described for coupling magnetite cores to G5-NH_2 PAMAM dendrimers, which in turn have been used for the in situ growth of plasmonic nanophases. Contrary to common routes found in the literature, where the PAMAM dendrimers are grown in situ at the surface of the magnetic nanoparticles,[21] herein, commercial high generation PAMAM dendrimers were conjugated to magnetic nanoparticles using distinct surface chemical modification routes. The strategies explored in this work describe an alternative route for the preparation of multifunctional materials containing dendrimers of higher generation (e.g., PAMAM G5), while reducing the number of preparative steps involved in the in situ divergent growth of the dendritic molecules over the magnetic phase. In line with this goal, Figure 1 illustrates the strategies investigated here to synthesize multifunctional dendrimer-based nanostructures.

Briefly, in Route 1, citrate coated Fe_3O_4 NPs were explored for the incorporation of the dendritic macromolecules by the conventional carbodiimide crosslinking chemistry. In this case, AuNPs were grown in situ without requiring additional reducing agents, where the citrate molecules and the PAMAM dendrimers aid in the reduction and growth kinetics of the plasmonic phase. Route 1 stands out for its simplicity as compared to the other routes. Hence, Route 2 introduces the one-step grafting of the PAMAM dendrimer to a magnetic core protected by a siliceous shell. This strategy promotes a more robust conjugation of the dendritic molecule to the magnetic phase, while allowing the entrapment of seed particles required for the nucleation of the plasmonic phase. This is demonstrated here by growing alloyed Au:Ag nanostructures with the dendrimer acting as reducing agent. In Route 3, the magnetite core was coated with several polyelectrolyte layers followed by crosslinking of PAMAM dendrimer-entrapped Au nanoparticles. The versatility of this method allows the controlled assembly of the plasmonic phase to the magnetic core in terms of available functional groups for the conjugation of Au DENPs (i.e., which increases with a greater number of polyelectrolyte layers) as well as the possibility to tune the SERS response as the distance of the plasmonic phase to the magnetic core increases (i.e., reduction of the attenuation effect caused by the magnetic core). Hence, these three chemical routes demonstrate the versatility of dendritic macromolecules, such as PAMAM dendrimers, in the preparation of multifunctional materials containing magnetic and a plasmonic phases depending on the envisaged application. As will be discussed below, this is an attractive aspect for SERS screening of target analytes by allowing the synthesis of hybrid materials with optical response based on the selected chemical route.

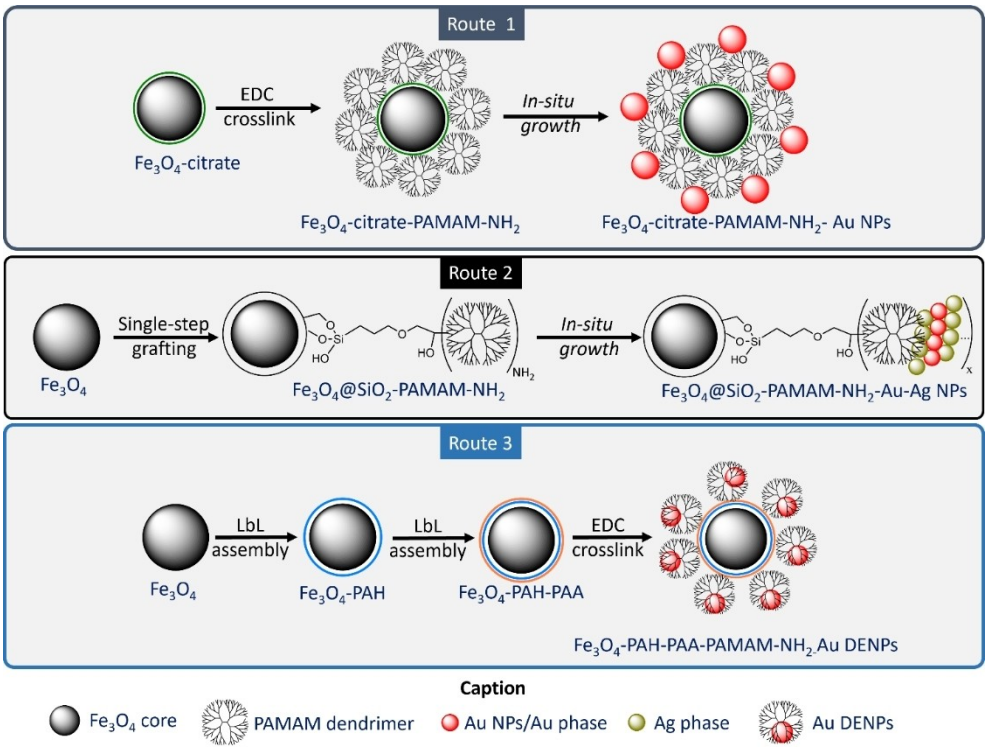

Figure 1. Surface chemical modification routes for preparing magneto-plasmonic dendrimer-based multifunctional structures: 1) citrate-activated conjugation using EDC as crosslinker; 2) conjugation onto silica shells by using an alkoxysilane coupling agent; 3) layer-by-layer polyelectrolyte assembly followed by EDC crosslinking. AuNPs = gold nanoparticles; Au-AgNPs = alloyed gold-silver nanoparticles; Au DENPs = Au dendrimer entrapped nanoparticles.

Route 1: Citrate activated conjugation using EDC as crosslinker

In route 1, citrate-capped Fe_3O_4 nanoparticles were firstly prepared, and then the G5-NH_2 PAMAM dendrimer was conjugated with Fe_3O_4 through EDC chemistry by crosslinking the primary amine terminal groups of PAMAM with the carboxylic acid groups of citrate.[22] Figure 2 shows the FTIR and zeta potential measurements of the resulting magnetic nanoparticles confirming the successful conjugation of the PAMAM dendrimer to the magnetite core. The FTIR spectrum of the Fe_3O_4-citrate nanoparticles shows the typical bands of citrate adsorbed on the surface of colloidal Fe_3O_4 nanoparticles (1630 and 1385 cm^{-1} region), which are attributed to the asymmetrical and symmetrical stretching modes $\nu_{as}(COO<C^{\cdot}>)$ and $\nu_s(COO<C^{\cdot}>)$, respectively.[17] The weak intensity of the citrate band has been previously attributed to the close-packed assembly of the stabilizing molecules at the surface of magnetite, resulting in constrained molecular motion.[17] In the FTIR of the final Fe_3O_4-citrate-PAMAM composite, the characteristic bands of the amide group (–CONH–) can be observed in the whole spectral region. Namely, the intense band at 1635 cm^{-1} (amide I) is associated with the C=O stretching vibration, while the amide II band at the 1550 cm^{-1} region is related to the in-plane C–N–H bending and C–N stretching.[23] The bands located 540 cm^{-1} are attributed to lattice Fe–O stretching of magnetite.[18b,24] Furthermore, the surface charge measurements further confirm the successful conjugation of the PAMAM dendrimer to the surface of the magnetite nanoparticles. Thus, the zeta potential measurements show an upper shift of the isoelectric point after dendrimer conjugation, which agrees with the presence of primary and tertiary amine groups with higher pK_a values.[25]

TEM analysis of the Fe_3O_4-citrate nanoparticles reveals that the particles display an average size of 30 nm ± 7 nm, in which the conjugation of the dendrimer did not result in significant morphological changes (Figure 3). The powder XRD analysis also confirms magnetite as the main phase showing the typical patterns of the cubic inverse spinel structure of Fe_3O_4 (JCPDS file no. 19-0629; Figure S1 in the Supporting Information).[26]

The magnetic profile of the Fe_3O_4-citrate nanoparticles before and after G5-NH_2 PAMAM conjugation is detailed in Figure 4. Both systems display magnetic hysteresis typical of magnetic nanoparticles with the size over the blocking radius at 300 K.[27] Moreover, the inset of Figure 4 shows that particles display a very small hysteresis loop, indicating low coercivity and remanence. The values of remanent magnetization (Mr), saturation of magnetization (Ms), and coercivity (Hc) are detailed in Table 1. The normalized Ms for the Fe_3O_4-citrate is 63 emu/$g_{Fe_3O_4}$, which is close to other reported values for similarly sized magnetite nanoparticles.[17] The conjugation of the PAMAM dendrimer resulted in the slight reduction of Ms to 49 emu/$g_{Fe_3O_4}$ due to the nonmagnetic layer at the particles' surface.[28] Despite this reduction, the particles still show enough magnetization that allows their fast collection (< 20 s) from an aqueous solution by applying an external magnetic gradient.

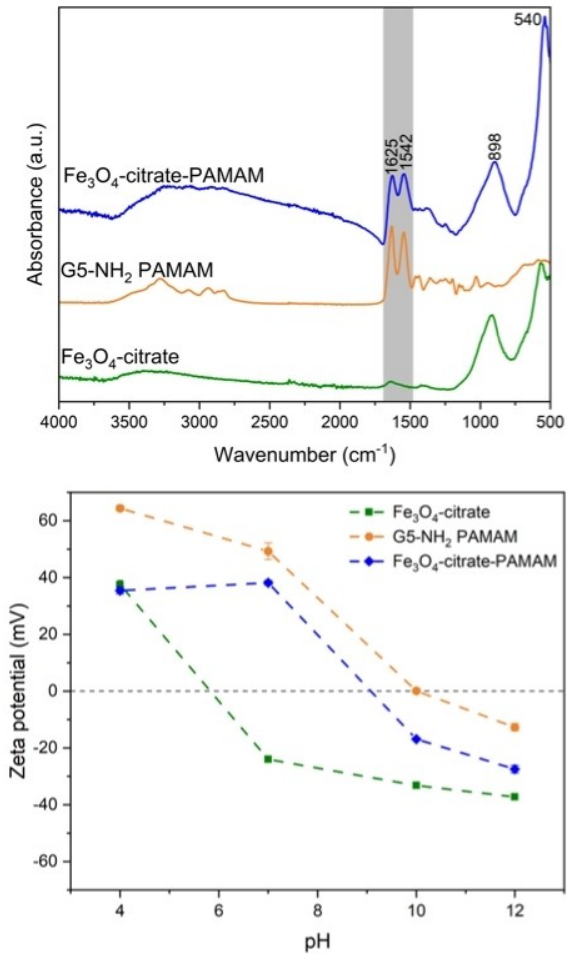

Figure 2. Top: FTIR-ATR spectra Fe_3O_4-citrate, G5-NH_2 PAMAM and Fe_3O_4-citrate-PAMAM-NH_2 (the band at 898 cm^{-1} arises from excess citrate and nitrate adsorbed to the surface of the particles). Bottom: zeta potential measurements of the corresponding colloids at different pH values.

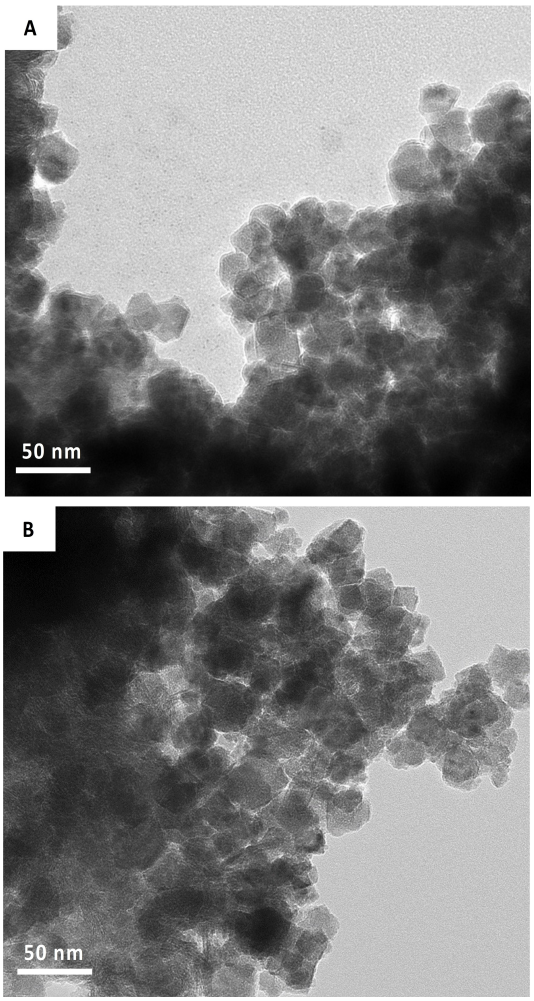

Figure 3. TEM micrographs of A) Fe_3O_4-citrate nanoparticles and B) the same particles after conjugation with G5-NH_2 PAMAM.

Route 2: Conjugation onto silica shells by using an alkoxysilane coupling agent

In this chemical strategy, the PAMAM dendrimers with amine groups were attached to amorphous SiO_2 shells previously grown over the Fe_3O_4 cores. The presence of the shells protects the magnetic core in harsher chemical environments and promotes long-term grafting of the dendrimer to the surface of the magnetic nanoparticles (e.g., minimizing possible leaching of the dendrimer at different chemical environments when compared with the particles from Route 1).[9b,29] In this case, the G5-NH_2 PAMAM was grafted to the surface of the magnetite nanoparticles in a single-step.

Figure 5 shows the FTIR-ATR spectra of the magnetic hybrid nanoparticles prepared through strategy 2. In Figure 5 (top), typical bands of the amide group (–CONH–) of the G5-NH_2 PAMAM dendrimer are observed at 1648 and 1625 cm^{-1}, confirming the successful grafting of the dendrimer to the magnetic core. Moreover, the band located at 1031 cm^{-1} (Si–O stretching vibration) along with the shift of the band located at

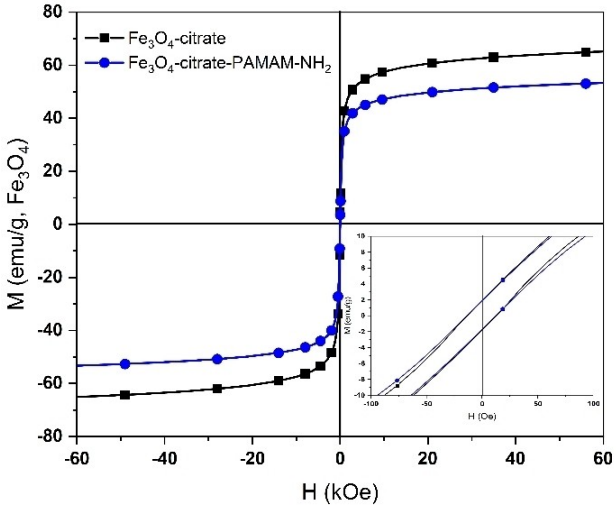

Figure 4. Magnetization hysteresis loop measured at 300 K for the Fe_3O_4-citrate nanoparticles and of the same particles after conjugation with G5-NH_2 PAMAM (M = magnetization and H = magnetic field strength).

Table 1. Summary of the relevant magnetic properties measured at 300 K of all magnetic systems investigated in this work.

Sample	Ms [emu/g_{sample}]	Ms [emu/$g_{Fe_3O_4}$]	Mr [emu/$g_{Fe_3O_4}$]	Hc (Oe, ±2)
Fe_3O_4-citrate	14	63	1.8	12
Fe_3O_4-citrate-PAMAM-NH_2	47	49	1.8	12
Fe_3O_4	80	86	3.4	65
Fe_3O_4@SiO_2-PAMAM-NH_2	75	89	11.4	89
Fe_3O_4@SiO_2-PAMAM-COOH	47	89	3.4	75
Fe_3O_4@PAH-PAA-2 L-PAMAM-NH_2	70	86	7.0	48
Fe_3O_4@PAH-PAA-4 L-PAMAM-NH_2	69	91	8.7	48
Fe_3O_4@PAH-PAA-6 L-PAMAM-NH_2	71	88	8.7	70

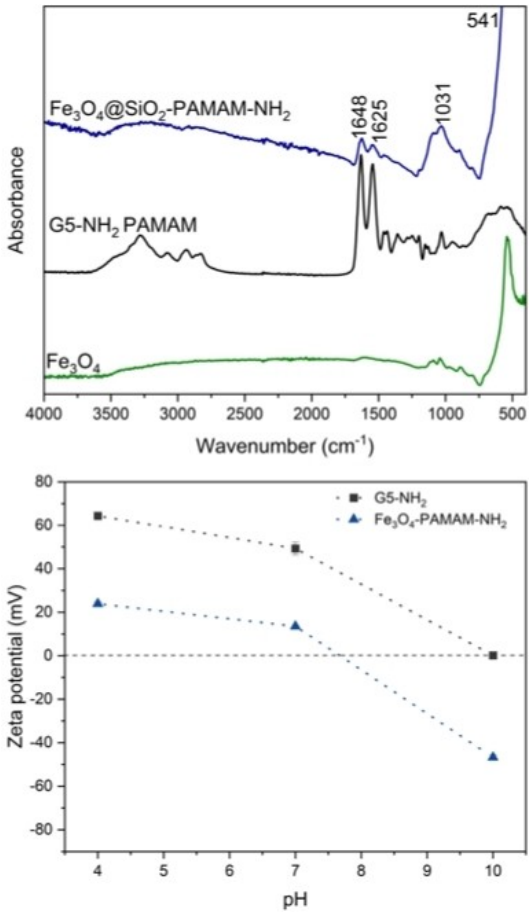

Figure 5. Top: FTIR-ATR spectra of Fe_3O_4 nanoparticles; G5-NH_2 PAMAM dendrimer; Fe_3O_4@SiO_2-PAMAM-NH_2 and bottom: zeta potential measurements of the Fe_3O_4@SiO_2-PAMAM-NH_2 hybrid nanoparticles. For comparative purposes the zeta potential measurements of the corresponding pristine dendrimers at the same pH values are also presented (lines are merely guides for the eye).

565 cm^{-1} (Fe O–Si bond) are indication for the presence of the silica shells.[30]

The surface charge measurements as a function of pH (Figure 5, bottom) further confirm the successful conjugation of the PAMAM dendrimers to the magnetic phase. At pH 7, the hybrids with the primary amine surface groups still present a positive surface charge, but as the pH increases, there is a shift of the zeta potential to negative values given the change in the protonation state of the primary amine groups of the dendrimer.

Figure 6 shows a TEM image of the final hybrid materials with G5-NH_2 PAMAM, where the magnetic core of the hybrid nanostructures displays a typical size of 47 nm ± 9 nm with a shell thickness of 3.4 nm ± 0.8 nm.

The magnetic profile of the intermediate magnetic nanoparticles and of the final hybrids is presented in Figure 7. All systems possess a magnetic hysteresis characteristic of ferrimagnetic materials with the size over the blocking radius at 300 K.[27] The inset of Figure 7 shows that the sample exhibits a small hysteresis loop, indicating low coercivity and remanence. The values of Mr, Ms, and Hc are detailed in Table 1. The normalized Ms for the Fe_3O_4 is 86 emu/g, which is close to the reported values for bulk magnetite and nanoparticles prepared through the same method.[18] The conjugation of the dendrimers did not induce any significant changes in the normalized magnetic profile of the hybrid materials, suggesting that after conjugation, the particles still retain a good magnetic response for facile separation from aqueous solutions.

Route 3: Layer-by-layer polyelectrolyte assembly followed by EDC crosslinking

This strategy employed magnetite cores like Route 2. However, the magnetic phase was previously coated with polyelectrolyte bilayers of PAH/PAA,[31] followed by conjugation of the G5-NH_2 PAMAM dendrimer through EDC chemistry. An excess of EDC was also used in this strategy to enable the crosslinking of the electrolyte shells and ensure greater chemical stability of the final material.[32] The layer-by-layer (LbL) assembly and shell crosslinking were monitored through FTIR and zeta potential measurements (Figure 8). The analysis of the FTIR spectra of the final magnetic materials confirms the successful conjugation of the G5-NH_2 PAMAM dendrimer as the final layer given the appearance of the typical amide I and amide II bands (1648 and 1625 cm^{-1}) of the dendrimer (dotted line, Figure 8h–j). In this work, EDC was also used to crosslink the PAH/PAA layers through the activation of the carboxylate moiety of PAA with the diimide of EDC, where the resulting intermediate species react more easily with the amine groups of PAH under mild conditions.[33] In this case, the crosslinking of the PAH/PAA layers was more difficult to monitor through FTIR as the amide bands of PAMAM appear in the same spectral region.[33,34]

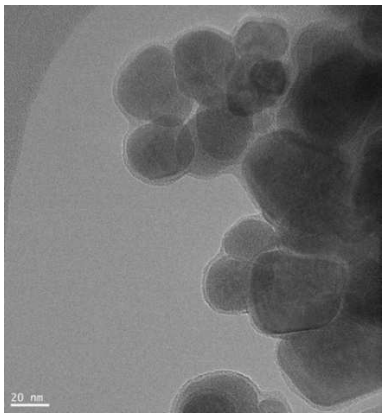

Figure 6. TEM image of Fe_3O_4@SiO_2-PAMAM-NH_2 particles detailing the siliceous outer shells.

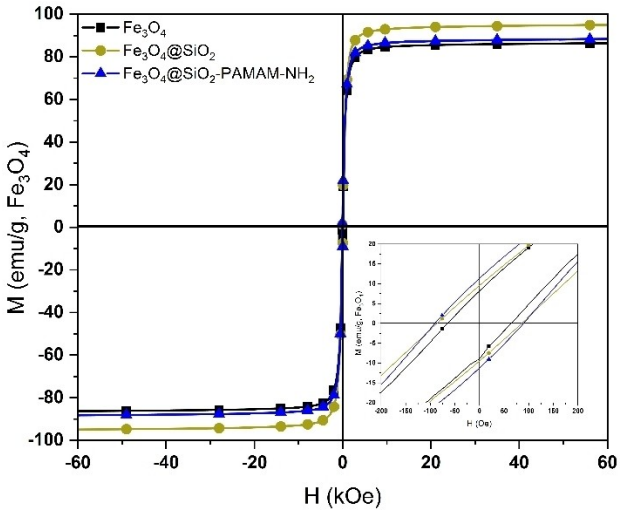

Figure 7. Magnetization hysteresis loop measured at 300 K for the Fe_3O_4, Fe_3O_4@SiO_2 and Fe_3O_4@SiO_2-PAMAM-NH_2 (M = magnetization and H = magnetic field strength).

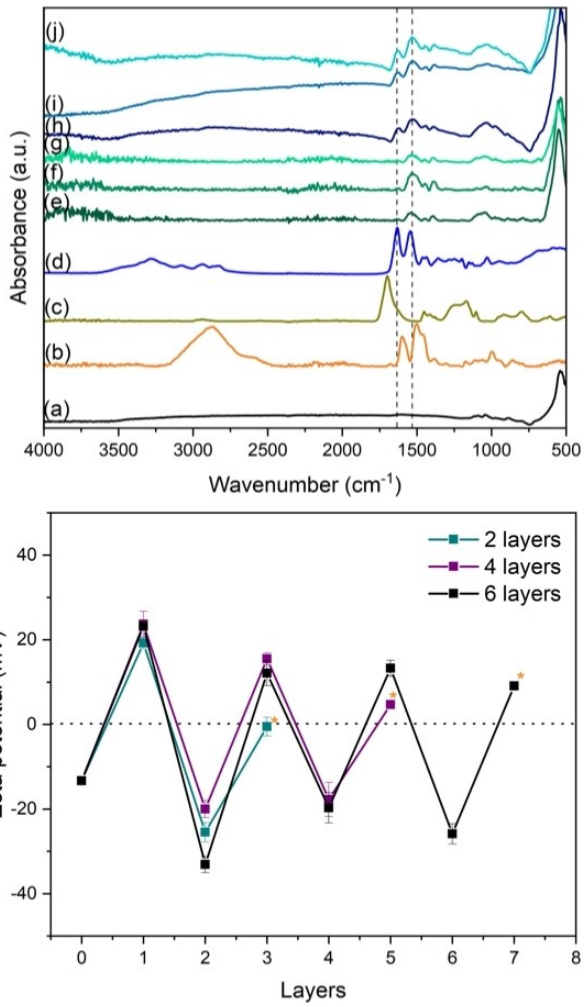

Figure 8. Top: FTIR-ATR spectra of a) Fe_3O_4; b) PAH; c) PAA; d) G5-NH_2-PAMAM; Fe_3O_4@LbL-PAH-PAA with e) 2, f) 4 or g) 6 layers and h)–j) Fe_3O_4@LbL-PAH-PAA-PAMAM-NH_2 of the corresponding particles. Bottom: Zeta potentials of each intermediate material at pH 6.6 until the final Fe_3O_4@LbL-PAH-PAA-PAMAM-NH_2 composite with 2, 4 and 6 polyelectrolyte layers (the asterisk marks the layer with the G5 NH_2 PAMAM).

Despite that, the bands located between 1600 and 1300 cm^{-1} in the Fe_3O_4@LbL-PAH-PAA composite materials (Figure 8e–g) are typical from the carboxyl and amine groups of the polyelectrolytes, indicating their assembly over the magnetic phase[32c]. In fact, after crosslinking, these bands ascribed to the presence of PAA and PAH tend to decrease in intensity due to the formation of the amide bond.[35] Moreover, the close inspection of the 1800–1200 cm^{-1} spectral region of the Fe_3O_4@LbL-PAH-PAA materials provide valuable information regarding the LbL assembly (Figure S2). Firstly, there is an almost complete disappearance of the band associated with the carboxylic acid group of PAA at 1700 cm^{-1} (Figure 8c) with the appearance of a new band at lower wavenumbers (1540 cm^{-1}) related to the vibrational mode $\nu_{as}(COO<C^{-}>$ of the carboxylate anion (Figure 8e–g). This suggests the predominance of the anionic form of PAA at the surface of the particles after the LbL assembly.[36] In addition, the small shoulder located at 1621 cm^{-1} may be attributed to the $\delta_{as}(NH_3^+)$ from the PAH polyelectrolyte as a consequence of the assembly and packing with PAA.[37] The prevalence of these charged species is essential for an optimal LbL assembly under buffered conditions.[37] Zeta potential measurements were used to monitor the LbL polyelectrolyte coating of the magnetic core. The alternating charge reversal observed at the end of each step confirms the successful electrostatic assembly of oppositely charge layers of polyelectrolytes. As expected, an increasing number of layers may result in reduced colloidal stability with formation of agglomerates.[32a] This was observed after the third layer, in which the net charge of the assemblies starts to decrease and becomes closer to zero.

The Fe_3O_4@LbL-PAH-PAA-PAMAM-NH_2 were also characterized by TEM imaging, as detailed in Figure 9. After layer-by-layer assembly, no significant changes were observed in any of the systems regarding the particle size and morphology of the magnetic core (47 nm ± 9 nm; Figure S3). Also, with an increas-

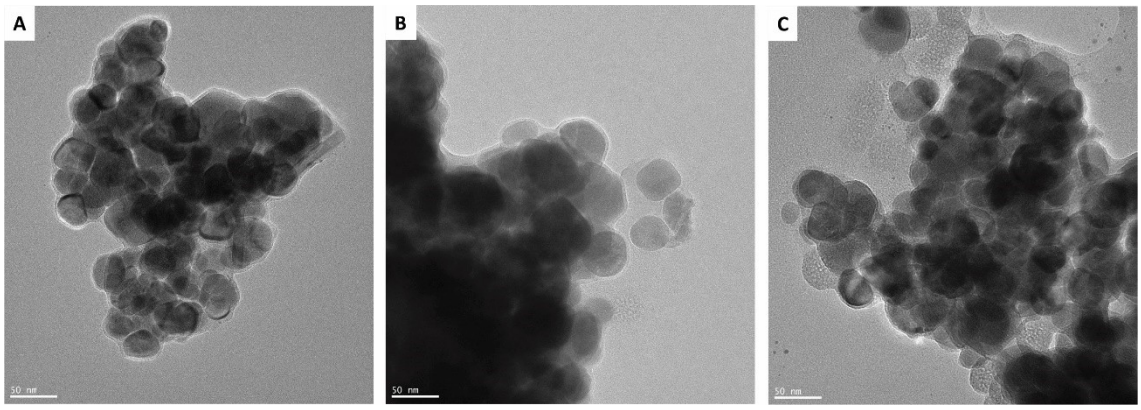

Figure 9. TEM images of Fe_3O_4@LbL-PAH-PAA-PAMAM-NH_2 composite materials with a) 2, b) 4, and c) 6 polyelectrolyte layers.

ing number of polyelectrolyte layers, a higher amount of organic content can be observed around the magnetic phase, confirming the successful assembly of the layers. The XRD analysis of the Fe_3O_4@LbL-PAH-PAA-PAMAM-NH_2 does not reveal any changes in the typical patterns of the cubic inverse spinel structure of Fe_3O_4 (JCPDS file no. 19-0629)[26] after functionalization (Figure S4). Considering the size of the particles and their magnetic profile (Figure 10), we suspect that the assembly of the layers occurs around multiple magnetic particles instead of each particle. However, the formation of the composite in this way does not seem to be critical to alter any of its magnetic properties or the applicability of this material for the purposes envisioned in this work.

The magnetic profile of the Fe_3O_4@LbL-PAH-PAA-PAMAM-NH_2 composite materials with a distinct number of polyelectrolyte layers is detailed in Figure 10. Like the previous strategy, all systems possess a magnetic hysteresis characteristic of ferrimagnetic materials with the size over the blocking radius at 300 K.[27] Moreover, all the materials display a small hysteresis loop, indicating low coercivity and remanence. The values of Mr, Ms, and Hc are detailed in Table 1. The non-normalized Ms values show that the particles containing the PAH/PAA-PAMAM-NH_2 assembly display a lower magnetization value due to the mass fraction corresponding to the nonmagnetic organic phase. However, this change does not affect the facile magnetic separation of the particles of the solution. Despite that, the normalized Ms values for the composite materials are close to the bare magnetite, suggesting that the assembly process does not significantly impact the magnetic properties of the final material.

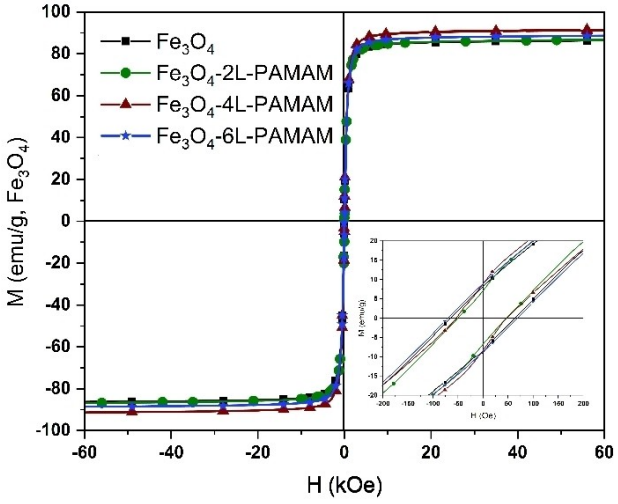

Figure 10. Magnetization hysteresis loop measured at 300 K for the Fe_3O_4 nanoparticles and the corresponding Fe_3O_4@LbL-PAH-PAA-PAMAM-NH_2 composite materials containing 2, 4, and 6 layers of polyelectrolyte (M = magnetization and H = magnetic field strength).

SERS studies of dendrimer-based multifunctional hybrid materials

In this research, the magneto-plasmonic materials were obtained by coupling plasmonic nanoparticles onto the above hybrid nanostructures. We expect that the distinct chemical surface modifications explored for the magnetic phase confer different behavior regarding the final arrangement of the plasmonic colloids. This is of great relevance for SERS applications using solid substrates because it is well known that their sensitivity is strongly dependent on the arrangement of metal particles over the surfaces. Figure 11 details the different types of dendrimer-based magneto-plasmonic nanostructures prepared in this work along with their corresponding TEM micrographs. These multifunctional materials were explored regarding their ability for the magnetic assisted uptake of the pesticide thiram from spiked water samples followed by in situ SERS screening. In the first study, the citrate-stabilized magnetite nanoparticles were prepared, and the G5-NH_2 PAMAM dendrimer was conjugated to the surface of the particles by crosslinking. The resulting magnetic materials were used as substrates for the in-situ growth of Au nanoparticles without adding any other reducing agent but the surface dendrimer macromolecules. The resulting magneto-plasmonic particles were then investigated to probe pesticide thiram dissolved in water.

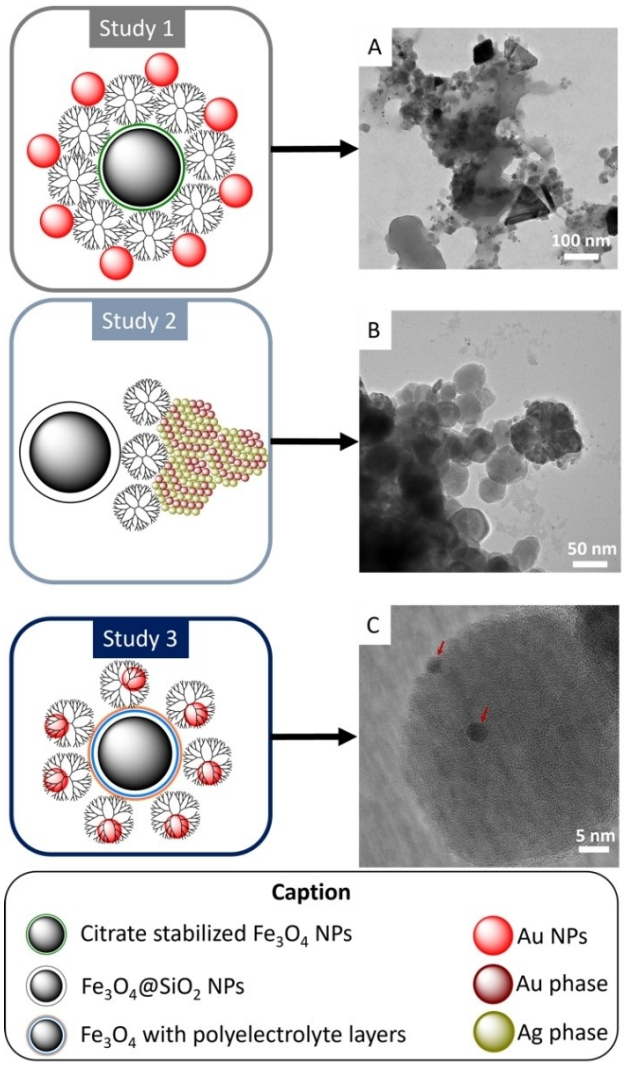

Figure 11. Dendrimer-based magneto-plasmonic nanostructures and their use as SERS substrates in different types of studies. A) Study 1: citrate-capped Fe_3O_4 PAMAM-NH_2 with Au DSNPs; B) Study 2: Fe_3O_4@SiO_2-PAMAM-NH_2 Au:Ag DSNPs; C) Study 3: Fe_3O_4@LbL-PAA/PAAH-PAMAM Au DENPs, the red arrows indicate the Au phase distributed along magnetite.

Table 2. Raman bands of thiram and corresponding assignments based on literature data.[38,39]

Raman [cm^{-1}]	SERS [cm^{-1}]	Assignments
–	1513w	ν(CN)
1458sh	–	$\delta_{as}(CH_3)$
1394w	–	ν(C–N)
1372w	1370–1380vs	$\delta_s(CH_3)$
1138w	1145w	ρ(CH_3) and ν(N–CH_3)
973 m	–	ν(C–S)
845	–	–CH_3 groups (several vibrational modes)
558vs	557–564w	ν_s(CSS) coupled to ν(S–S)
437 m	–	δ(CSS) and δ(CNC)
390 s	–	ν(S–S)
358w		$\nu(CH_3–NC)$

vs: very strong; s: strong; m: medium; w: weak; vw: very weak; sh: shoulder

Table 2 indicates the Raman bands of thiram, which have been assigned according to reported literature data.[38,39] As detailed in Figure 12, after incubation for 30 minutes, the Fe_3O_4-citrate-PAMAM-Au magneto-plasmonic nanoparticles display the SERS bands of thiram, suggesting that the resulting composite can be effectively used to probe thiram at the concentration of 100 μM. The dissociation of dithiocarbamate molecules such as thiram is essential for their successful SERS detection.[38] Consequently, the marked decrease in intensity of the band located at 559 cm^{-1} confirms the cleavage of the disulfide bond at the Au surface. This is further confirmed by the absence, in the SERS spectrum, of the band at 390 cm^{-1}, which is related to the S–S stretching vibration. In addition, the presence of the shoulder at 1513 cm^{-1} in the three SERS spectra

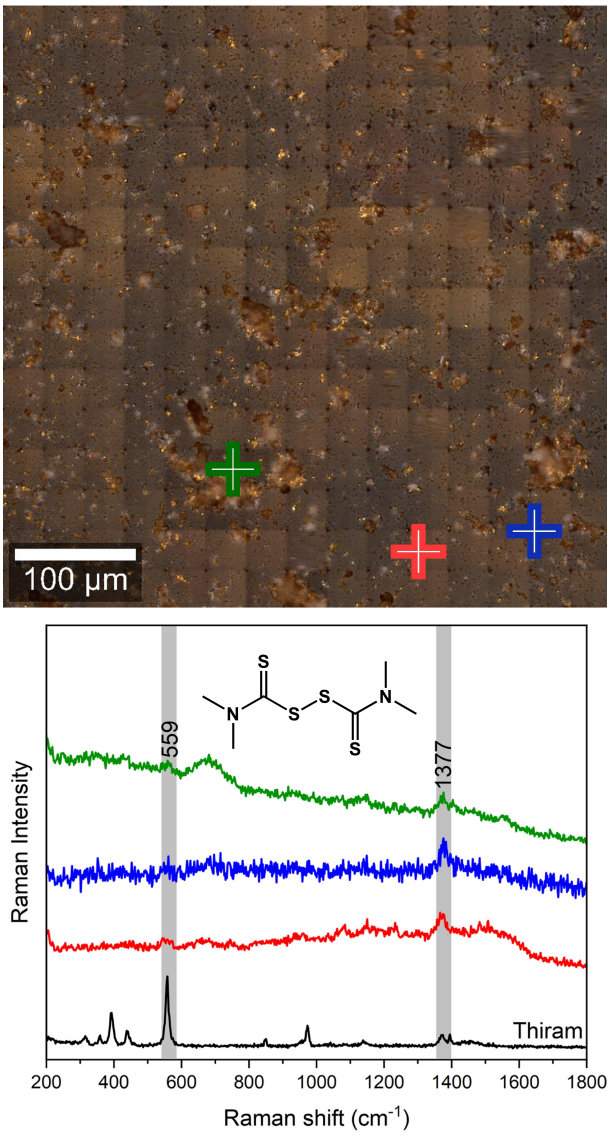

Figure 12. SERS experiments using Fe_3O_4-citrate-PAMAM-AuNPs to probe thiram at 100 μM. Top: Optical microscopy image of the magneto-plasmonic substrates and bottom: the corresponding SERS spectra at the marked points. For comparative purposes, the Raman spectrum of thiram powder is also presented. Note that the band located at ~650 cm^{-1} is due to magnetite.

emphasizes the hypothesis of the prevalence of the thioureide tautomer as the main adsorbate to the surface of the Au nanophases.[38] The enhancement of the band at 1386 cm^{-1} arises from the short distance of the CH_3 and CN groups to the metal surface.[38] No SERS activity was observed for concentrations lower than 100 μM. These magneto-plasmonic nanostructures show polydispersity which might explain the variability of the Raman signal, thus indicating lack of homogeneity for trace concentrations in the pesticide. The observed morphological heterogeneity of AuNPs can be due to the reduction process employed during the in situ synthesis of the AuNPs. The conjugated presence of citrate and PAMAM can result in different kinetics for Au nanoparticle formation,[40] ensuing structures with multiple sizes and shapes as detailed Figure 11.

In the second study, the Fe_3O_4@SiO_2-PAMAM-NH_2 hybrids were used for the in situ growth of alloyed Au:Ag nanoparticles. We have used in this case metal alloys just to demonstrate the feasibility of this approach when using other plasmonic nanostructures. However, like the procedure reported above, no additional reducing agents were used besides the PAMAM dendrimer present at the particles' surfaces. Figure 13 shows the SERS activity of the Fe_3O_4@SiO_2-PAMAM-NH_2-Au:Ag magneto-plasmonic substrates for probing thiram. Similarly, to the previous case, the pronounced decrease of the band intensity at 564 cm^{-1} indicates the molecular breakdown of thiram as the primary mechanism for probing this dithiocarbamate. Moreover, in some of the SERS spectra, a shoulder at 1512 cm^{-1} is observed, indicating the predominance of thioureide tautomer as the main adsorbate on the metallic surface.[38] No SERS signal was observed for analyte concentrations below 1 mM of thiram, thus indicating lower SERS sensitivity of the substrates as compared to the previous ones. This behavior can be explained by the relative heterogeneity of the metal particles over the magnetite nanoparticles, rather than the use of the Au:Ag alloy instead of Au. In fact, in our previous research it was demonstrated that Au:Ag colloids show comparable or superior SERS sensitivity as compared to monophase Au generated in situ in the presence of the PAMAM dendrimer.[40] In addition, other effects may arise which influence the SERS activity of the Fe_3O_4@SiO_2-PAMAM-NH_2-Au-Ag (1:1) hybrid nanoparticles. Namely, during the in situ growth of the plasmonic phase, the influence of the magnetic phase over the Au:Ag nanoparticle growth cannot be disregarded, which leads to different optical profile of the final hybrid material when compared with Au:Ag colloids prepared in the sole presence of the dendrimer. Moreover, taking in consideration that the reaction parameters between both Route 1 and Route 2 are quite different, the variable noble metal loading can also contribute for different SERS activities. Nevertheless, Figure 13 shows that the magneto-plasmonic systems prepared by Route 2 can be used as SERS probing systems, opening a new opportunity for research in this type of dendrimer-based multifunctional materials.

In the third scenario, dendrimer-entrapped Au nanoparticles (Au DENPs) were coupled to magnetite nanoparticles by conjugation onto the surfaces previously coated with polyelectrolytes layers (PAH/PAA). For comparative purposes, bare

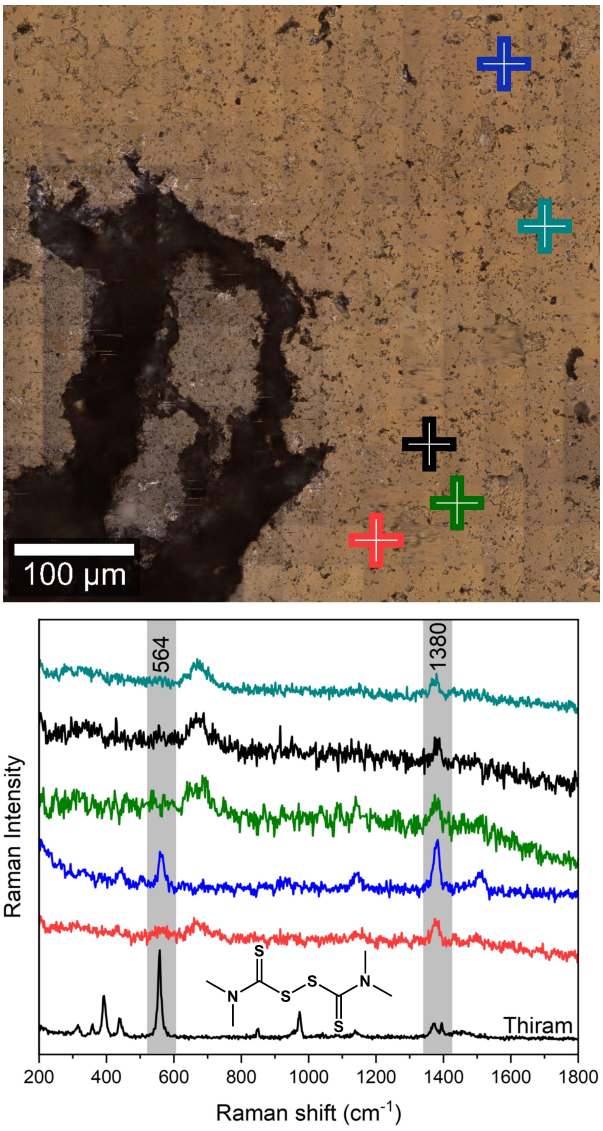

Figure 13. Results of SERS experiments using Fe_3O_4@SiO_2-PAMAM-NH_2-Au-Ag (1:1) nanoparticles to probe thiram at 1 mM. Top: Optical microscopy image of the magneto-plasmonic substrates and bottom: the corresponding SERS spectra at the marked points. For comparative purposes, the Raman spectrum of thiram powder is also presented.

magnetite nanoparticles were also assembled with the Au DENPs, that is, in the absence of polyelectrolytes. In this study, the Au DENPs were firstly prepared by adding an additional reducing agent,[19] and then the resulting plasmonic nanoparticles were crosslinked with the magnetic phase. Figures S5 and S6 show the UV/VIS spectra and TEM images for these nanostructures, highlighting the presence of the dendrimer entrapped Au nanoparticles.

Figure 14 shows the SERS spectra of thiram when probed by using Fe_3O_4@LbL-PAH/PAA-PAMAM-Au nanostructures having a variable number of polyelectrolyte layers. These experiments indicate an improvement of the SERS signal by increasing the number of layers around the magnetic core, which can be due to attenuation of the absorbing effect of the

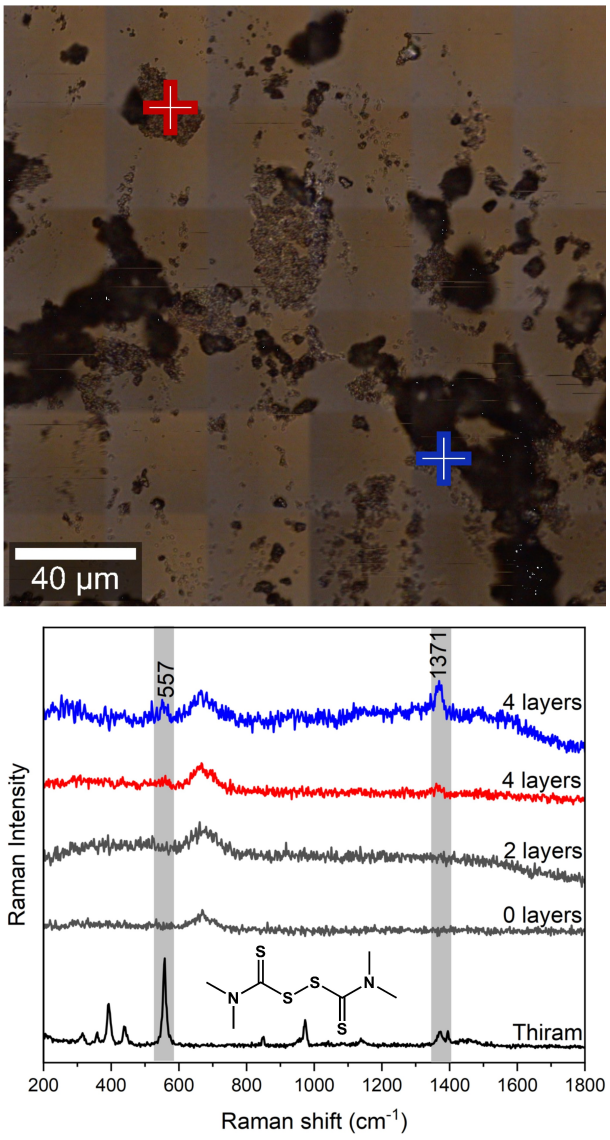

Figure 14. Preliminary SERS experiments using Fe_3O_4@LbL-PAH/PAA-PAMAM-AuNPs to probe thiram at 100 µM. Top: Optical microscopy image of the magneto plasmonic substrate with 4 layers of PAH/PAA and bottom: the corresponding SERS spectra at the marked points. The Raman spectrum of thiram powder and the typical SERS spectra of the magneto-plasmonic with 0 and 2 layers are presented for comparative purposes.

magnetite cores.[41] The lower concentration of thiram probed in these experiments was 100 µM, thus comparable to nanostructures prepared by the methods described above.

Table 3 provides examples of reported magneto-plasmonic materials with their SERS sensitivity for probing analytes of diverse chemical nature. The main objective of this table is to provide a concise overview of the materials investigated to date and how they compare between each other, highlighting some of their important features. However, caution should be present in doing a direct comparison in terms of SERS activity between the indicated systems. Indeed, different operational probing conditions and Raman setups have been used in these studies (e.g., type of incident laser, laser power, or focal configurations). Although there are magneto-plasmonic systems reported in the literature with better SERS sensitivity, the systems reported here also detected a low amount of thiram and, in addition, provide versatility for combining magnetic and plasmonic nanophases. Thus, the strategies reported herein contribute for the design of magneto-plasmonic nanostructures whose SERS response can be further optimized for specific analytical contexts.

Conclusions

We have explored three chemical routes to conjugate G5 PAMAM dendrimers to cores containing magnetite nanoparticles. The ensuing dendrimer-based magnetic materials were fully characterized, confirming the successful conjugation of PAMAM dendrimers to the magnetic core through each one of the strategies explored: crosslinking, chemical grafting, or layer-by-layer assembly. These hybrid nanostructures were then used as platforms to grow plasmonic nanoparticles, which were then applied in proof-of-principle experiments to demonstrate their feasibility as magneto-plasmonic substrates for SERS applications such as monitoring water quality. Overall, all the magneto-plasmonic nanostructures displayed SERS activity for probing samples of thiram dissolved in water at concentrations as low as 100 µM, after their adsorption and magnetic separation from spiked aqueous samples. However, the multiple chemical surface modifications confer distinct potential on the resulting SERS substrates depending on the envisaged uses. Hence, the crosslinking strategy (Route 1) stands for simplicity of preparation compared to the other routes. Among the routes investigated, chemical grafting of the dendrimer onto SiO_2 outer shells (Route 2) is the most laborious but it is the elective option for SERS analysis of aqueous samples in which magnetite is susceptible to leaching. This was clearly observed in the magnetization decrease for the magnetite samples not coated with SiO_2 shells. Finally, layer-by-layer assembly offers unmatched versatility regarding the final architecture and composition of the hybrid nanostructures, such as for the type of particle morphology and the distance of the plasmonic particles from the magnetic cores. In this regard, coupling magnetic phases on plasmonic nanostructures with tunable composition and integration into lab-on-a-chip devices could be a major advance for ultrasensitive SERS analysis.[43] Further research could unlock the full potential of these materials by testing their SERS activity by using other molecular probes and more complex aqueous matrices.

Experimental Section

Materials

The following chemicals were used without further treatment: G5-NH_2 PAMAM dendrimers in methanol (Dendritech, Midland, MI, USA); ferrous sulfate heptahydrate ($FeSO_4 \cdot 7H_2O$, >99%, Panreac); Sodium citrate tribasic dihydrate ($C_6H_9Na_3O_9$, >99%, Sigma-Aldrich), potassium hydroxide (KOH, >86%, Pronolab); sodium hydroxide (NaOH, >99%, JMGS); potassium nitrate (KNO_3, >99%,

Table 3. Concise overview of magneto-plasmonic materials reported to date based on ferrite cores for SERS screening applications.

Magnetic phase	Plasmonic phase	Target analyte/reporter	SERS limit of detection	Main features	Ref.
Fe_3O_4 + PA-MAM-NH_2	variable Au/Ag phases	thiram	1×10^{-4} M	Multiple chemical strategies for the conjugation of Fe_3O_4 NPs with several plasmonic phases of Au/Ag. PAMAM dendrimer facilitate the combination of magnetic and plasmonic phases and provides additional chemical functionality. High magnetization of the NPs allows their fast separation for subsequent SERS probing of adsorbed thiram.	this work
$Fe_{3-x}O_4$@SiO_2	star-shaped Au shell	thiram	1×10^{-8} M	$Fe_{3-x}O_4$ multicores coated with SiO_2 and Au branched shells. Good magnetization allows the magnetic assisted uptake of sorbents and in situ SERS screening of thiram.	[42a]
Fe_3O_4@SiO_2-PAMAM-NH_2	star-shaped AuNPs	ziram/thiram	1×10^{-5} M	Hybrid magnetic nanoparticles containing PAMAM dendrimer which promotes the entrapment of Au seeds for posterior anisotropic growth into nanostars. Multiple operational Raman setups which allow the probing of ziram/thiram under different analytical conditions (e.g., solid state, solution or *in loco* using a portable Raman device).	[42b]
Fe_3O_4@PEI	spherical AuNPs	tetracycline (TC)	1×10^{-8} M	Multilayer encapsulation of Fe_3O_4 and Au nanoparticles assisted by PEI. Magnetic assisted uptake of TC and SERS sensing up to 10 nM.	[8b]
Fe_3O_4	spherical AuNPs	penicillin G (PG)	1×10^{-4} M	Seed-mediated growth of AuNPs with different sizes. Magnetic assisted uptake of PG and variable SERS response depending on the size of the plasmonic phase.	[42c]
Fe_3O_4	Spherical AgNPs	4-mercaptobenzoic acid	2×10^{-3} M	Magneto-plasmonic material obtained by the physical blending of Fe_3O_4 and AgNPs. Ability to tune the amount of deposited AgNPs during the blending process. Magnetic assisted SERS sensing resulting on improved response than the equivalent bare AgNPs.	[42d]
Fe_3O_4@SiO_2	Au shell with different morphologies	2-mercaptopyrimidine	1×10^{-8} M	Spiky or bumpy Au shells grown in situ on silica coated magnetite cores. The SERS activity is still observed for at least 1 month, despite the morphological changes of the material. The topographical properties of the shell provide variable SERS response, where more anisotropic shells provide improved results.	[42e]
Fe_3O_4 chains	Au@Ag nanoflowers	rhodamine 6G (R6G) and monitoring of catalytic reduction of 4-nitrothiophenol	R6G: 1×10^{-11} M	1D magneto-plasmonic nanochains were obtained by magnetic field assembly of Fe_3O_4@AuNPs. In situ growth of Ag phase results in Fe_3O_4@SiO_2@Au@Ag nanoflowers in magneto-plasmonic chains. High SERS sensitivity for probing the dye R6G, with the possibility to also monitor the catalytic reduction of 4-nitrothiophenol.	[42f]
Fe_3O_4 stabilized with oleic acid	Au nanostars capped with polystyrene (PS)	Malachite Green (MG) and Crystal Violet (CV)	MG: 5×10^{-9} M CV: 1×10^{-8} M	Co-encapsulation of plasmonic and magnetic phases driven by self-assembly of PS capped Au nanostars and Fe_3O_4 NPs stabilized by oleic acid. The previous assembly was further encapsulated by block copolymers resulting on colloidal particle clusters. Magnetically assisted pre-concentration results on good SERS response for the trace probing of organic dyes.	[42 g]
ZrO_2@$CoFe_2O_4$	clusters of spherical AuNPs	thiolated MG (SERS reporter)	–	Mesoporous ZrO_2 NPs were firstly loaded with magnetic $CoFe_2O_4$ NPs and then with AuNPs by laser ablation. The resulting magneto-plasmonic clusters can be used for the magnetic assisted SERS sorting of target analytes based on the response of a reporter molecule.	[42 h]

Sigma-Aldrich); ethanol (CH_3CH_2OH, >99%, Panreac); tetraethyl orthosilicate (TEOS, $Si(OC_2H_5)_4$, >99%, Sigma-Aldrich); 3-(glycidyloxypropyl)trimethoxysilane (GLYMO, $C_9H_{20}O_5Si$, >98%, Sigma-Aldrich); 3-aminopropyltriethoxysilane (APTES, $C_9H_{23}NO_3Si$, ≥98.0%, Sigma-Aldrich); ammonia solution (NH_4OH, 25%, Riedel-de-Häen); *N*-(3-dimethylaminopropyl)-*N*-ethylcarbodiimide (EDC, $C_8H_{17}N_3$, ≥97%, Sigma-Aldrich); *N*-hydroxysuccinimide (NHS, $C_4H_5NO_3$, ≥97%, Sigma-Aldrich); tetrachloroauric(III) acid trihydrate ($HAuCl_4\cdot3H_2O$, 99.9%, Sigma-Aldrich); poly(allylamine hydrochloride) (PAH, $[CH_2CH(CH_2NH_2\cdot HCl)]_n$, $M_w\approx17500$, Sigma-Aldrich), polyacrylic acid (PAA, $(C_3H_4O_2)_n$, $M_w\approx1800$, Sigma-Aldrich); phosphate-buffered saline (PBS tablets, Sigma-Aldrich, pH 7.4); (*N*-morpholino)ethanesulfonic acid (MES, $C_6H_{13}NO_4S$, >99%, Sigma-Aldrich); thiram ($C_6H_{12}N_2S_4$, ≥98.0%, Sigma-Aldrich). All the aqueous solution were prepared using ultrapure water (18.2 MΩ·cm, 25 °C, MilliQ, Millipore). ***CAUTION!*** thiram is a biocide that should be handled in small amounts and under adequate safety conditions due to its toxicity. Waste should be placed in containers for further treatment and disposal.

Synthesis of nanomaterials

Citrate-capped Fe_3O_4 nanoparticles and conjugation to PAMAM: Citrate capped magnetite nanoparticles were prepared according to a previously reported procedure with some modifications.[17] Briefly, 882 mg of citrate, 480 mg of sodium hydroxide, and 51 g of sodium nitrate were mixed in 80 mL of ultrapure water. This mixture was mechanically stirred (700 rpm) at 100 °C until a translucid solution was obtained. Then, 1.2 mL of an aqueous solution of $FeSO_4 \cdot 7H_2O$ (1 M) was injected into the above solution, and the reaction was left to proceed at 100 °C with mechanical stirring for 1 h. After that time, the resulting particles were collected magnetically and washed with ultrapure water. The black solid was then left to dry at 40 °C. The PAMAM dendrimer was conjugated with the magnetic nanoparticles by dispersing 40 mg of Fe_3O_4 along with 80 mg of PAMAM dendrimer on MES buffer at pH 6. The resulting mixture was then mechanically dispersed at 900 rpm, room temperature, for 15 min. After that time, 150 mg of EDC and 60 mg of NHS were added to the previous mixture, and the reaction was left to proceed for 24 h while keeping the mechanical stirring. The resulting particles were then collected magnetically, washed with ultrapure water, and left to dry at 40 °C.

Fe_3O_4@SiO_2-PAMAM-NH_2 hybrid nanostructures: The magnetite core was obtained following the oxidative hydrolysis of $FeSO_4 \cdot 7H_2O$ under alkaline conditions.[18] To 25 mL of deoxygenated water, 1.90 g of KOH and 1.52 g of KNO_3 were added, and the resulting mixture was heated to 60 °C with N_2 bubbling and with mechanical stirring at 500 rpm. After complete dissolution, 25 mL of an aqueous solution containing $FeSO_4 \cdot 7H_2O$ was slowly added, and the stirring was increased to 700 rpm. The resulting solution displayed a dark-green color after adding the whole Fe^{II} precursor. This mixture was left to react for 30 minutes. After that time, the resulting product was placed at 90 °C with N_2 bubbling for 4 h without stirring. The resulting black powder was then extensively washed with deoxygenated water and ethanol and dried by evaporating the solvent. The G5-NH_2 PAMAM dendrimer was conjugated to the magnetite core in a single step with the simultaneous formation of the siliceous shell. To this end, 100 mg of PAMAM dendrimer were dispersed in 45 mL of ultrapure water, and the pH was adjusted to 12 using 5 M NaOH. Then, 50 mg of the prepared Fe_3O_4 nanoparticles were dispersed in the dendrimer solution at 40 °C with mechanical stirring (900 rpm). After dispersion, 260 μL of GLYMO and 260 μL of TEOS were sequentially added, and the reaction was left to proceed for 7 h. After that time, the particles were collected magnetically and extensively washed with ethanol. The resulting black solid was then left to dry at 40 °C.

Layer-by-layer assembly of PAMAM dendrimers onto Fe_3O_4: The magnetic core was prepared following the same procedure detailed in Section 4.2.2. Then 40 mg of negatively charged Fe_3O_4 nanoparticles were firstly dispersed in 25 mL of a PAH aqueous solution (2.5 mg/mL in PBS, pH 6.6, 0.5 M NaCl) for the deposition of the first layer. The resulting mixture was left to incubate for 30 min at room temperature with vertical rotation (200 rpm). After that time, the particles were collected magnetically and washed with ultrapure water. Then, the second layer was added by dispersing the Fe_3O_4-PAH nanoparticles again in 25 mL of PAA aqueous solution (5 mg/mL, pH 6.6, 0.5 M NaCl). The magnetic nanoparticles were then left to incubate with PAA for 30 minutes at room temperature and with vertical rotation (200 rpm). The resulting particles were then collected magnetically and washed with ultrapure water to obtain the Fe_3O_4-PAA-PAH nanoparticles protected by two layers of polyelectrolyte. The same procedure was sequentially repeated to obtain magnetic nanoparticles with 4 and 6 layers. The G5-NH_2 PAMAM dendrimer was then conjugated with each magnetic system containing 2, 4, and 6 layers. To this end, 40 mg of Fe_3O_4 with 2, 4, or 6 layers of PAA/PAH were dispersed in 30 mL of PBS, pH 6.6, 0.5 M of NaCl. Then 80 mg G5-NH_2 PAMAM were added along with 160 mg of EDC and 60 mg of NHS. The reaction was left to proceed at room temperature for 24 h with vertical rotation (200 rpm). After that time, the magnetic particles were separated magnetically and extensively washed with ultrapure water.

Citrate-capped Fe_3O_4 PAMAM-NH_2 conjugates with Au: The Au nanoparticles were grown in situ using the Fe_3O_4-PAMAM-NH_2 nanoparticles prepared in Section 4.2.1. Consequently, 10 mg of Fe_3O_4-citrate-PAMAM nanoparticles were dispersed in 29 mL of ultrapure water for 5 min. Then, the particles were placed at 90 °C with mechanical stirring (700 rpm) for 15 min. After that time, 1.5 mL of an aqueous solution of $HAuCl_4 \cdot 3H_2O$ (65 mg in 2.3 mL) was injected into the Fe_3O_4-citrate-PAMAM dispersion. The reaction was left to proceed at 90 °C for 24 h while keeping the mechanical stirring. After that time, the particles were collected magnetically, extensively washed with ultrapure water, and left to dry at 40 °C.

Fe_3O_4@SiO_2-PAMAM-NH_2 Au/Ag magneto-plasmonic systems: The magnetic particles containing the G5-NH_2 PAMAM dendrimer described in Section 4.2.2 were used for the in-situ growth of Au:Ag alloy nanoparticles with a molar ratio of 10:10:1 Au:Ag:PAMAM. To this end, 16 mg of Fe_3O_4@SiO_2-PAMAM-NH_2 nanoparticles were dispersed in 20 mL of ultrapure water at 800 rpm (mechanical stirring), 35 °C for 15 min. After that time, 200 μL of an aqueous solution of $AgNO_3$ (227.3 mM) and 1.8 mL of an aqueous solution of $HAuCl_4 \cdot 3H_2O$ (25.38 mM) were sequentially added, and the reaction was left to proceed for 24 h. Then, the particles were collected magnetically, extensively washed with ultrapure water, and left to dry at 30 °C.

Fe_3O_4@LbL-PAA/PAAH-PAMAM Au magneto-plasmonic systems: The Fe_3O_4@LbL-PAA-PAH nanoparticles were prepared according to the procedure reported in Section 4.2.3. However, in this case, the G5-NH_2 PAMAM dendrimer was conjugated only after the encapsulation of Au nanoparticles in a prior step.[19] Consequently, the PAMAM dendrimer entrapped Au nanoparticles (Au DENPs) were firstly prepared by dispersing 30 mg of G5-NH_2 PAMAM dendrimer in 9.5 mL of methanol. Then, an aqueous solution of $HAuCl_4 \cdot 3H_2O$ in a 200:1 molar ratio Au:PAMAM was added in dropwise fashion under vigorous stirring. The coordination of the Au(III) in the interior of the PAMAM dendrimer was allowed to proceed for 30 min. After that time, an ice-cold solution of sodium borohydride (24 mg in 3.70 mL of ultrapure water and 1.30 mL of methanol) was added. The reaction was left to proceed for 2 h at room temperature with magnetic stirring. After 2 h, the resulting PAMAM entrapped Au nanoparticles were dialyzed against ultrapure water for 3 days (six times, 4 L). The dendrimer entrapped Au nanoparticles were then conjugated with the Fe_3O_4@LbL-PAA/PAH by adding 10 mL of PAMAM-Au to 5 mg Fe_3O_4@LbL nanoparticles containing 2 or 4 layers. The resulting mixtures were left to incubate for 30 min at room temperature with vertical rotation (200 rpm). Then, the resulting particles were collected magnetically, washed with ultrapure water, and redispersed in 5 mL MES buffer (pH 5.5). To the resulting mixture, 20 mg of EDC was added to crosslink the Au DENPs to the Fe_3O_4@LbL-PAA-PAH nanoparticles. The reaction was left to proceed with vertical rotation (100 rpm) at room temperature overnight.

SERS experiments: The SERS studies were performed by dispersing the dendrimer-based magnetoplasmonic nanoparticles (0.5 mg) to aqueous solutions of thiram (5 mL) with different concentrations (1 mM to 100 μM). The mixtures were incubated for thirty minutes at 25 °C ± 1 °C, using a vertical rotor (200 rpm) to promote the adsorption of thiram to the surfaces of the Au/Ag nanophases. After that time, the samples were separated magnetically from the solution using a Nd-Fe-B magnet, and the nanoparticles were

washed once with ultrapure water. The substrates were transferred to glass sides for SERS analysis and left to dry at room temperature.

Instrumentation: Transmission electron microscopy (TEM) micrographs were obtained using the STEM HD2700 electron microscope operating at 200 kV. Samples for electron microscopy were prepared by diluting the original colloids and depositing them on a carbon-coated Cu grid. The reported nanoparticle average sizes were determined by measuring at least 100 individualized particles identified among multiple TEM images. Fourier transform infrared (FTIR) spectra of all the systems were acquired over the range of 4000–450 cm^{-1} using a Bruker Optics Tensor 27 spectrometer coupled to a horizontal attenuated total reflectance (ATR) cell. The samples were placed on the ATR crystal, and 512 scans were acquired at 4 cm^{-1} resolution.

The magnetic profile of the samples was determined using the Quantum Design MPMS3 SQUID magnetometer, as a function of the applied magnetic field (from +50 to −50 kOe), at 300 K. Geometrical effects were corrected using the methodology described in ref. [20]. Additional measurements were also performed using a paramagnetic standard to correct the remanent fields of superconducting coil.

To estimate the Fe_3O_4 content for each sample, all the materials were analyzed using atomic absorption spectrophotometry (AAS) using the Perkin Elmer Analyst 100 apparatus. The X-ray powder diffraction (XRD) data were obtained using the PANalytical Empyrean X-ray diffractometer equipped with a Cu–Kα monochromatic radiation source at 45 kV/40 mA. The UV/VIS spectra were acquired using the GBC Cintra-303 UV–VIS spectrophotometer. The surface charge of the nanoparticles was determined by zeta potential measurements through electrophoretic light scattering performed using a Zetasizer Nano ZS instrument equipped with a He:Ne laser operating at 633 nm and a scattering detector at 173°, from Malvern Instruments. Raman imaging studies were accomplished using a combined Raman AFM-SNOM confocal microscope WITec alpha300 RAS+ with a He:Ne laser sample excitation source operating at 633 nm (0.2 mW) with a spot size of 858 nm. All the SERS spectra were obtained with 30 acquisitions for 0.5 s each. The spectra were built based on an analyzed area of 30×30 μm where the points giving rise to the best SERS signal were selected.

Acknowledgements

T. F. thanks the Fundação para a Ciência e Tecnologia (FCT) for PhD grant SFRH/BD/130934/2017. A. L. D.-d.-S. acknowledges FCT for a research contract under the Program "Investigador FCT" 2014. This work was developed within the scope of the project CICECO-Aveiro Institute of Materials, UIDB/50011/2020, UIDP/50011/2020 and LA/P/0006/2020, financed by national funds through the FCT/MEC (PIDDAC).

Conflict of Interest

The authors declare no conflict of interest.

Data Availability Statement

The data that support the findings of this study are available in the supplementary material of this article.

Keywords: colloids · dendrimers · magneto-plasmonic · nanoparticles · Raman spectroscopy

[1] J. G. Ovejero, S. J. Yoon, J. Li, A. Mayoral, X. Gao, M. O'Donnell, M. A. García, P. Herrasti, A. Hernando, *Microchim. Acta* **2018**, *185*, 130.
[2] a) T. T. Nguyen, F. Mammeri, S. Ammar, *Nanomaterials* **2018**, *8*, 149; b) I. Mukha, O. Chepurna, N. Vityuk, A. Khodko, L. Storozhuk, V. Dzhagan, D. R. T. Zahn, V. Ntziachristos, A. Chmyrov, T. Y. Ohulchanskyy, *Nanomaterials* **2021**, *11*, 1113; c) H. Ilkhani, C.-J. Zhong, M. Hepel, *Nanomaterials* **2021**, *11*, 1326; d) K.-H. Huynh, E. Hahm, M. S. Noh, J.-H. Lee, X.-H. Pham, S. H. Lee, J. Kim, W.-Y. Rho, H. Chang, D. M. Kim, A. Baek, D.-E. Kim, D. H. Jeong, S.-m. Park, B.-H. Jun, *Nanomaterials* **2021**, *11*, 1215.
[3] P. C. Pinheiro, A. L. Daniel-da-Silva, H. I. S. Nogueira, T. Trindade, *Eur. J. Inorg. Chem.* **2018**, *30*, 3443–3461.
[4] S. Scaramuzza, S. Polizzi, V. Amendola, *Nanoscale Adv.* **2019**, *1*, 2681–2689.
[5] a) C. Daruich De Souza, B. Ribeiro Nogueira, M. E. C. M. Rostelato, *J. Alloys Compd.* **2019**, *798*, 714–740; b) V. Amendola, R. Pilot, M. Frasconi, O. M. Marago, M. A. Iatì, *J. Phys. Condens. Matter* **2017**, *29*, 203002.
[6] a) Z. Wang, L. Ma, *Coord. Chem. Rev.* **2009**, *253*, 1607–1618; b) S. Zeng, K.-T. Yong, I. Roy, X.-Q. Dinh, X. Yu, F. Luan, *Plasmonics* **2011**, *6*, 491; c) F. Dumur, E. Dumas, C. R. Mayer, *Nanomaterials* **2020**, *10*, 548.
[7] J. Ovejero, P. Herrasti, in *Nanohybrids: Future Materials for Biomedical Applications*, "Hybrid Magneto-plasmonic Nanoparticles in Biomedicine: Fundamentals, Synthesis and Applications" (Eds.: G. Sharma, A. García-Peñas), **2021**, pp. 1–54.
[8] a) P. C. Pinheiro, S. Fateixa, H. I. S. Nogueira, T. Trindade, *Nanomaterials* **2019**, *9*, 31; b) P. C. Pinheiro, S. Fateixa, A. L. Daniel-da-Silva, T. Trindade, *Sci. Rep.* **2019**, *9*, 19647; c) X. Hou, X. Wang, R. Liu, H. Zhang, X. Liu, Y. Zhang, *RSC Adv.* **2017**, *7*, 18844–18850; d) V. N. Archana, S. A. Sam, A. P. Balan, M. R. Anantharaman, *J. Magn. Magn. Mater.* **2021**, *536*, 168092.
[9] a) A. G. Niculescu, C. Chircov, A. M. Grumezescu, *Methods* **2022**, *199*, 16–27; b) A. Spoială, C.-I. Ilie, L. N. Crăciun, D. Ficai, A. Ficai, E. Andronescu, *Appl. Sci.* **2021**, *11*, 11075.
[10] a) R. Hao, R. Xing, Z. Xu, Y. Hou, S. Gao, S. Sun, *Adv. Mater.* **2010**, *22*, 2729–2742; b) K. Mylkie, P. Nowak, P. Rybczynski, M. Ziegler-Borowska, *Materials* **2021**, *14*, 248; c) A. L. Daniel-da-Silva, T. Trindade, in *Surface Chemistry of Colloidal Nanocrystals*, Royal Society of Chemistry, **2021**, p. 1–46.
[11] M. Mehdipour, L. Gloag, D. Hagness, J. Lian, M. S. Alam, X. Chen, R. D. Tilley, J. J. Gooding, *Part. Part. Syst. Charact.* **2022**, *39*, 2200051.
[12] a) C. Song, M. Shen, J. Rodrigues, S. Mignani, J.-P. Majoral, X. Shi, *Coord. Chem. Rev.* **2020**, *421*, 213463; b) T. Fernandes, A. L. Daniel-da-Silva, T. Trindade, *Coord. Chem. Rev.* **2022**, *460*, 214483.
[13] a) M. Kavitha, M. R. Parida, E. Prasad, C. Vijayan, P. C. Deshmukh, *Macromol. Chem. Phys.* **2009**, *210*, 1310–1318; b) W. Song, L. Ding, Y. Chen, H. Ju, *Chem. Commun.* **2016**, *52*, 10640–10643; c) A. J. Ruiz-Sanchez, C. Parolo, B. S. Miller, E. R. Gray, K. Schlegel, R. A. McKendry, *J. Mater. Chem. B* **2017**, *5*, 7262–7266; d) B. Devadas, A. P. Periasamy, K. Bouzek, *Coord. Chem. Rev.* **2021**, *444*, 214062; e) J. Guerra, A. C. Rodrigo, S. Merino, J. Tejeda, J. C. García-Martínez, P. Sánchez-Verdú, V. Ceña, J. Rodríguez-López, *Macromolecules* **2013**, *46*, 7316–7324; f) Y. Fan, W. Sun, X. Shi, *Small Methods* **2017**, *1*, 1700224; g) J. Li, M. Shen, X. Shi, *ACS Appl. Bio Mater.* **2020**, *3*, 5590–5605; h) S. Saedi, J.-W. Rhim, *Food Packag. Shelf Life* **2020**, *24*, 100473.
[14] M. Ma, Y. Yang, W. Li, R. Feng, Z. Li, P. Lyu, Y. Ma, *J. Mater. Sci.* **2019**, *54*, 323–334.
[15] L. Kannappan, R. Rajmohan, P. Edwin, *Mater. Lett.* **2021**, *301*, 130257.
[16] H. Cai, K. Li, M. Shen, S. Wen, Y. Luo, C. Peng, G. Zhang, X. Shi, *J. Mater. Chem.* **2012**, *22*, 15110–15120.
[17] C. Hui, C. Shen, T. Yang, L. Bao, J. Tian, H. Ding, C. Li, H. J. Gao, *J. Phys. Chem. C* **2008**, *112*, 11336–11339.
[18] a) R. Oliveira-Silva, J. Pinto da Costa, R. Vitorino, A. L. Daniel-da-Silva, *J. Mater. Chem. B* **2015**, *3*, 238–249; b) T. Fernandes, S. F. Soares, T. Trindade, A. Daniel-da-Silva, *Nanomaterials* **2017**, *7*, 68.
[19] R. Guo, H. Wang, C. Peng, M. Shen, M. Pan, X. Cao, G. Zhang, X. Shi, *J. Phys. Chem. C* **2010**, *114*, 50–56.
[20] C. O. Amorim, F. Mohseni, R. K. Dumas, V. S. Amaral, J. S. Amaral, *Meas. Sci. Technol.* **2021**, *32*, 105602.
[21] a) A. Zarei, S. Saedi, F. Seidi, *J. Inorg. Organomet. Polym. Mater.* **2018**, *28*, 2835–2843; b) M. Ghoochian, H. A. Panahi, S. Sobhanardakani, L. Taghavi, A. H. Hassani, *Microchem. J.* **2019**, *145*, 1231–1240; c) K. Lakshmi, R. Rangasamy, *J. Mol. Struct.* **2021**, *1224*, 129081; d) Y. Wang, P. Su, S. Wang, J. Wu, J. Huang, Y. Yang, *J. Mater. Chem. B* **2013**, *1*, 5028–

5035; e) S. Ekinci, Z. İlter, S. Ercan, E. Çınar, R. Çakmak, *Heliyon* **2021**, *7*, e06600.
[22] S. Lu, X. Li, J. Zhang, C. Peng, M. Shen, X. Shi, *Adv. Sci.* **2018**, *5*, 1801612.
[23] a) Y. Borodko, C. M. Thompson, W. Huang, H. B. Yildiz, H. Frei, G. A. Somorjai, *J. Phys. Chem. C* **2011**, *115*, 4757–4767; b) C. S. Camacho, M. Urgellés, H. Tomás, F. Lahoz, J. Rodrigues, *J. Mater. Chem. B* **2020**, *8*, 10314–10326.
[24] a) R. D. Waldron, *Phys. Rev.* **1955**, *99*, 1727–1735; b) H. Namduri, S. Nasrazadani, *Corros. Sci.* **2008**, *50*, 2493–2497.
[25] P. K. Maiti, R. Messina, *Macromolecules* **2008**, *41*, 5002–5006.
[26] Joint Committee for Powder Diffraction Studies, JCPDS, card no. 19-0629.
[27] A. G. Kolhatkar, A. C. Jamison, D. Litvinov, R. C. Willson, T. R. Lee, *Int. J. Mol. Sci.* **2013**, *14*, 15977–16009.
[28] a) S. Aliannejadi, A. H. Hassani, H. A. Panahi, S. M. Borghei, *Microchem. J.* **2019**, *145*, 767–777; b) Y. Zhou, L. Luan, B. Tang, Y. Niu, R. Qu, Y. Liu, W. Xu, *Chem. Eng. J.* **2020**, *398*, 125651.
[29] K. Cendrowski, P. Sikora, B. Zielinska, E. Horszczaruk, E. Mijowska, *Appl. Surf. Sci.* **2017**, *407*, 391–397.
[30] a) P. I. Girginova, A. L. Daniel-da-Silva, C. B. Lopes, P. Figueira, M. Otero, V. S. Amaral, E. Pereira, T. Trindade, *J. Colloid Interface Sci.* **2010**, *345*, 234–240; b) R. A. Bini, R. F. C. Marques, F. J. Santos, J. A. Chaker, M. Jafelicci, *J. Magn. Magn. Mater.* **2012**, *324*, 534–539; c) K. Rajkumari, J. Kalita, D. Das, S. L. Rokhum, *RSC Adv.* **2017**, *7*, 56559–56565; d) S. F. Soares, C. O. Amorim, J. S. Amaral, T. Trindade, A. L. Daniel-da-Silva, *J. Environ. Chem. Eng.* **2021**, *9*, 105189.
[31] a) Y. Guo, W. Geng, J. Sun, *Langmuir* **2009**, *25*, 1004–1010; b) A. Jafari, H. Sun, B. Sun, M. A. Mohamed, H. Cui, C. Cheng, *Chem. Commun.* **2019**, *55*, 1267–1270.
[32] a) S. H. Wang, X. Shi, M. Van Antwerp, Z. Cao, S. D. Swanson, X. Bi, J. R. Baker Jr., *Adv. Funct. Mater.* **2007**, *17*, 3043–3050; b) X. Shi, S. H. Wang, S. D. Swanson, S. Ge, Z. Cao, M. E. Van Antwerp, K. J. Landmark, J. R. Baker Jr, *Adv. Mater.* **2008**, *20*, 1671–1678; c) L. Xu, F. Lv, Y. Zhang, X. Luan, Q. Zhang, Q. An, *J. Phys. Chem. C* **2014**, *118*, 20357–20362.
[33] P. Schuetz, F. Caruso, *Adv. Funct. Mater.* **2003**, *13*, 929–937.
[34] A. Schneider, G. Francius, R. Obeid, P. Schwinté, J. Hemmerlé, B. Frisch, P. Schaaf, J.-C. Voegel, B. Senger, C. Picart, *Langmuir* **2006**, *22*, 1193–1200.
[35] a) J. L. Stair, J. J. Harris, M. L. Bruening, *Chem. Mater.* **2001**, *13*, 2641–2648; b) A. Chunder, S. Sarkar, Y. Yu, L. Zhai, *Colloids Surf. B* **2007**, *58*, 172–179.
[36] J. Choi, M. F. Rubner, *Macromolecules* **2005**, *38*, 116–124.
[37] F. Tristán, G. Palestino, J. L. Menchaca, E. Pérez, H. Atmani, F. Cuisinier, G. Ladam, *Biomacromolecules* **2009**, *10*, 2275–2283.
[38] S. Sánchez-Cortés, M. Vasina, O. Francioso, J. V. García-Ramos, *Vib. Spectrosc.* **1998**, *17*, 133–144.
[39] a) T. Fernandes, S. Fateixa, M. Ferro, H. I. S. Nogueira, A. L. Daniel-da-Silva, T. Trindade, *J. Mol. Liq.* **2021**, *337*, 116608; b) T. Fernandes, N. C. T. Martins, S. Fateixa, H. I. S. Nogueira, A. L. Daniel-da-Silva, T. Trindade, *J. Colloid Interface Sci.* **2021**, *612*, 342–354.
[40] a) J. D. S. Newman, G. J. Blanchard, *Langmuir* **2006**, *22*, 5882–5887; b) F. Avila-Salas, R. I. Gonzalez, P. L. Rios, I. Araya-Duran, M. B. Camarada, *J. Chem. Inf. Model.* **2020**, *60*, 2966–2976; c) G. Villaverde-Cantizano, M. Laurenti, J. Rubio-Retama, R. Contreras-Cáceres in *Reducing Agents in Colloidal Nanoparticle Synthesis*, "Reducing Agents in Colloidal Nanoparticle Synthesis: An Introduction", (Ed.: S. Mourdikoudis), The Royal Society of Chemistry, **2021**, pp. 1–27.
[41] C.-J. Yu, S.-M. Wu, W.-L. Tseng, *Anal. Chem.* **2013**, *85*, 8559–8565.
[42] a) T. T. Nguyen, S. Lau-Truong, F. Mammeri, S. Ammar, *Nanomaterials* **2020**, *10*, 294; b) T. Fernandes, N. C. T. Martins, A. L. Daniel-da-Silva, T. Trindade, *Spectrochim. Acta Part A* **2022**, *283*, 121730; c) P. C. Pinheiro, S. Fateixa, T. Trindade, *Magnetochemistry* **2017**, *3*, 32; d) L. Mikoliunaite, M. Talaikis, A. Michalowska, J. Dobilas, V. Stankevic, A. Kudelski, G. Niaura, *Nanomaterials* **2022**, *12*, 2860; e) E. E. Bedford, C. Méthivier, C.-M. Pradier, F. Gu, S. Boujday, *Nanomaterials* **2020**, *10*, 2136; f) Q. Ding, H. Zhou, H. Zhang, Y. Zhang, G. Wang, H. Zhao, *J. Mater. Chem. A* **2016**, *4*, 8866–8874; g) A. La Porta, A. Sánchez-Iglesias, T. Altantzis, S. Bals, M. Grzelczak, L. M. Liz-Marzán, *Nanoscale* **2015**, *7*, 10377–10381; h) A. Del Tedesco, V. Piotto, G. Sponchia, K. Hossain, L. Litti, D. Peddis, A. Scarso, M. Meneghetti, A. Benedetti, P. Riello, *ACS Appl. Nano Mater.* **2020**, *3*, 1232–1241.
[43] a) X. Wang, G. Ma, A. Li, J. Yu, Z. Yang, J. Lin, A. Li, X. Hanb, L. Guo, *Chem. Sci.* **2018**, *9*, 4009–4015; b) A. Li, X. Wang, L. Guo, S. Li, *J. Phys. Chem. C* **2019**, *123*, 25394–25401.

Manuscript received: July 31, 2022
Accepted manuscript online: September 9, 2022
Version of record online: October 1, 2022